Supplementary Information

Continuous Solar-driven Recycling of Lithium-ion Battery Cathode Materials Enabled by A Stable Benzobisthiazole-linked Polymeric Photocatalyst

Xiaohan Yu[1,2], Yuhua Fu[1,2], Jingfan Shao[1,2], Yuchen Yan[1,2], Jingya Xin[1,2], Jicheng Xu[1,2], Wei Huang[1,2]*, Yanguang Li[1,2]*

1. Institute of Functional Nano & Soft Materials (FUNSOM), Soochow University, Suzhou 215123, China.

2. Jiangsu Key Laboratory of Advanced Negative Carbon Technologies, Soochow University, Suzhou 215123, China.

Email: yanguang@suda.edu.cn; weihuang@suda.edu.cn

Table of contents

Supplementary Details

Supplementary Figures

Supplementary Details

Materials

N,N-dimethylformamide (DMF, 99.5%), 1,4-dioxane (≥99.5%), dichloromethane (DCM, 99%), *o*-dichlorobenzene (*o*-DCB, 98%), *n*-butyl alcohol (*n*-BuOH, 99.5%), hydrogen peroxide (H_2O_2, 30 wt% in water), methanol (MeOH, 99.9%), tetrahydrofuran (THF, 99.5%), ethanol (EtOH, 99.8%), 1-octanol (99.5%), acetic acid (≥99.8%), sulfuric acid (H_2SO_4, 98%), ammonium iron (II) sulfate hexahydrate ($Fe(NH_4)_2(SO_4)_2 \cdot 6H_2O$, 99.9%), xylenol orange (99.9%), D-sorbitol (≥99.5%), anhydrous potassium carbonate (K_2CO_3, 99.5%), sodium carbonate (99.99%), sodium hydroxide (NaOH, 99%), and tetrakis(triphenylphosphine)palladium ($Pd(PPh_3)_4$, 99.9%) were purchased from Macklin Biochemical Co., Ltd, Shanghai, China. Oxalic acid (≥99%), 4-formylphenylboronic acid (≥97%), 2,3,6,7,10,11-hexabromotriphenylene (HBTP, ≥98%), 2,5-diamino-1,4-benzenedithiol dihydrochloride (DABDT, ≥97%), and *p*-phenylenediamine (PDA, ≥99%) were purchased from Aladdin Reagent Co., Ltd., Shanghai, China. All the solvents and chemicals were used without further purification. Deionized water was prepared using a Milli-Q purification system.

Material synthesis

Synthesis of 2,3,6,7,10,11-hexakis(4-formylphenyl)triphenylene (HFPTP)

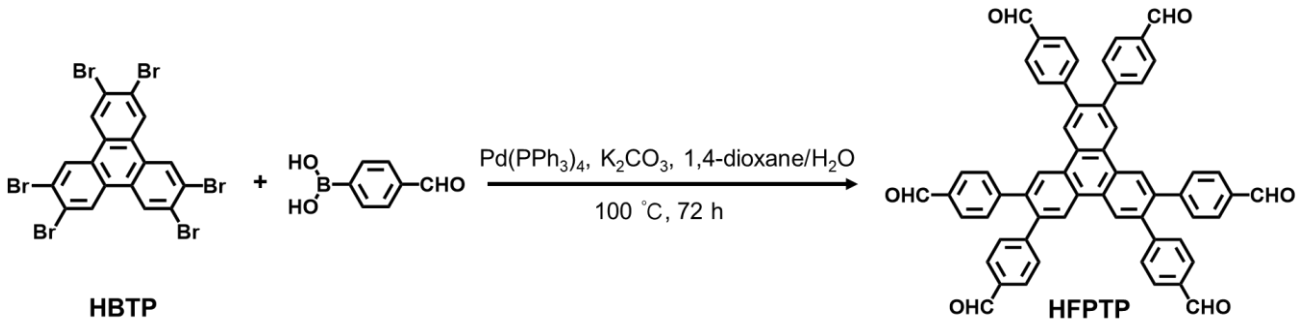

HFPTP was synthesized according to a previously reported procedure with slight modifications (*Angew. Chem. Int. Ed.* **2019**, *58*, 15922-15927). Typically, HBTP (1.4 g, 2 mmol), 4-formylphenylboronic acid (3.0 g, 20 mmol), anhydrous K_2CO_3 (2.5 g, 18 mmol), and $Pd(PPh_3)_4$ (693.0

mg, 0.6 mmol) were dissolved in a mixture solvent of 1,4-dioxane (130 mL) and H_2O (30 mL) in a 250 mL three-neck flask. The resulting solution was degassed by bubbling argon for 30 min, then heated at 100 °C for 72 h under an argon atmosphere. After cooling to room temperature, the resulting precipitate was collected by filtration and washed thoroughly with H_2O and MeOH. The crude product was further purified by silica gel column chromatography (DCM: ethyl acetate = 19 : 1) to afford HFPTP as a yellow powder (yield: 84%). ^{1}H NMR (400 MHz, $CDCl_3$) δ (ppm) = 10.05 (s, 6H), 8.79 (s, 6H), 7.87 (d, 12H), 7.52 (d, 12H); ^{13}C NMR (DMSO-d_6,400 MHz) δ (ppm) = 190.6, 145.8, 138.3 134.2, 129.7, 128.7, 128.4, 124.8 (Supplementary Fig. 24 and Fig. 25).

Characterizations

Fourier-transform infrared (FT-IR) spectra were collected on a Bruker Vertex 70 FTIR spectrometer under the attenuated total reflection (ATR) mode. Liquid ^{1}H and ^{13}C nuclear magnetic resonance (NMR) spectra were recorded using a 400 MHz Bruker Avance NMR spectrometer. Cross-polarized magic angle spinning (CP-MAS) solid-state ^{13}C spectra were collected using a 400 MHz Bruker Avance III solid-state NMR spectrometer equipped with a standard 4 mm magic angle spinning (MAS) double resonance probe head. Powder X-ray diffraction (XRD) was conducted on a PANalytical X-ray diffractometer with monochromatic Cu Kα radiation. X-ray photoelectron spectroscopy (XPS) results were obtained on an Ultra DLD X-ray photoelectron spectrometer. Scanning electron microscopy (SEM) images were taken on a ZEISS Gemini 500 scanning electron microscope. High-resolution transmission electron microscopy (TEM) images and energy-dispersive X-ray spectroscopy (EDS) measurements were carried out on a Thermo Scientific Talos F200X scanning/transmission electron microscope at 200 kV. Ultraviolet-visible (UV-vis) diffuse reflectance spectra were recorded on a Perkin Elmer Lambda 950 spectrophotometer using $BaSO_4$ as a reference. N_2 sorption experiments were carried out using a Micrometrics ASAP 2020 HD88 surface area and porosimetry analyzer. Samples were degassed at 120 °C under vacuum for 12 h before analysis. Thermogravimetric analysis

(TGA) was conducted on a Mettler Toledo TGA/DSC1 thermal analyzer under N_2 with the temperature ramped from 25 °C to 800 °C at a rate of 10 °C min^{-1}. Electron paramagnetic resonance (EPR) data were recorded on a JEOL JES-X320 electron spin resonance (ESR) spectrometer with or without visible light irradiation ($\lambda > 420$ nm). The concentrations of metal ions in the leachate were determined using inductively coupled plasma optical emission spectrometry (ICP-OES) on a PerkinElmer Avio 200 ICP optical emission spectrometer.

Chemical stability assessments

Chemical stability tests were carried out by dispersing 20 mg of TpTz or TpIm in 20 mL of 2 M HCl or 2 M NaOH. The suspensions were stirred continuously under ambient air at 80°C for 48 h. After cooling to room temperature, the solids were isolated via centrifugation, thoroughly washed with H_2O and EtOH, and then dried under vacuum at 80°C. The recovered samples were characterized by FT-IR spectroscopy to evaluate structural integrity.

Determination of H_2O_2 concentration

The H_2O_2 concentration was determined using the xylenol orange/Fe^{2+} colorimetric method, as previously reported in our work (*Nat. Commun.* **2024**, *15*, 8023). In this assay, H_2O_2 oxidizes Fe^{2+} to Fe^{3+}, which subsequently forms a purple complex with xylenol orange, exhibiting a characteristic absorbance at 580 nm (Equations 1 and 2).

$$2Fe^{2+} + H_2O_2 + 2H^+ \rightarrow 2Fe^{3+} + 2H_2O \quad (1)$$

$$Fe^{3+} + \text{xylenol orange} \rightarrow \text{purple complex} \quad (580\ \text{nm}) \quad (2)$$

The xylenol orange/Fe^{2+} colorimetric reagent was prepared by dissolving $Fe(NH_4)_2(SO_4)_2 \cdot 6H_2O$ (19.6 mg), D-sorbitol (3.6 mg), xylenol orange (14.3 mg), ethanol (2 mL) and H_2SO_4 (2 M, 2.5 mL) in deionized water to a final volume of 200 mL. For H_2O_2 detection, 50 μL of the sample solution (diluted if needed) was mixed with 10 mL of the freshly prepared xylenol orange reagent. The concentration

of H_2O_2 was determined by measuring the absorbance at 580 nm via UV-vis spectroscopy, based on a calibration curve constructed from standard H_2O_2 solutions (Supplementary Fig. 26).

Disassembly of commercial lithium-ion Batteries (LIBs)

The disassembly of spent commercial LIBs was carried out according to previously reported procedures (*Nat. Energy* **2023**, 8, 1137-1144). Specifically, the LIBs were fully discharged by immersion in 10% (w/v) NaCl solution for 12 h, followed by rinsing with ultrapure water and drying at 60°C. The battery cells were then manually disassembled in a fume hood by removing the outer casing and the aluminum-plastic film, after which the internal components (including the anode, cathode and separator) were carefully separated. The cathode film was flattened and cut into small pieces. The black mass was then stripped from the aluminum current collector and ground into a fine powder using a mortar and pestle for the leaching experiments.

Supplementary Figures

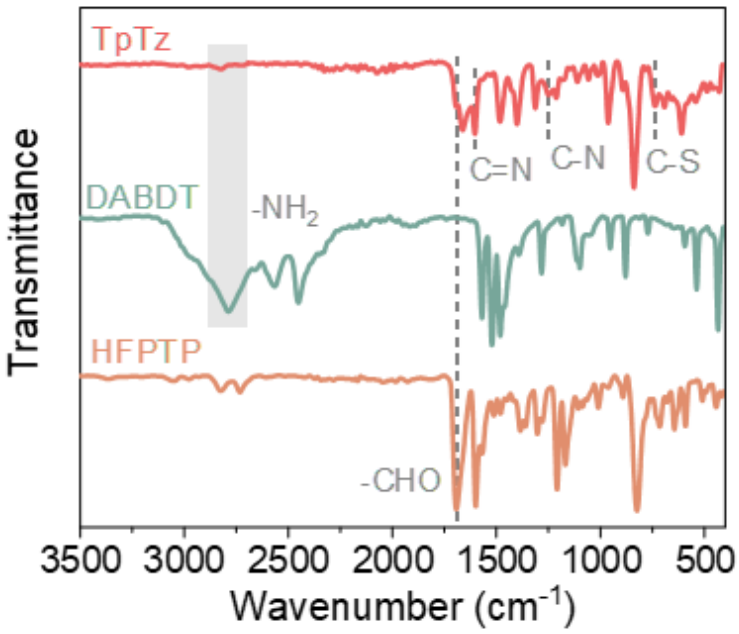

Supplementary Fig. 1 | FT-IR spectra of TpTz and corresponding monomer precursors.

Compared to the spectra of the monomer precursors, the FT-IR spectrum of TpTz exhibits three new absorption bands at 1606, 1248 and 693 cm^{-1}, corresponding to the characteristic stretching vibrations of C=N, C-N and C-S bonds in thiazole units, respectively. The substantial attenuation of signals associated with terminal aldehyde (1693 cm^{-1}) and amine (2789 cm^{-1}) functionalities indicates complete polymerization.

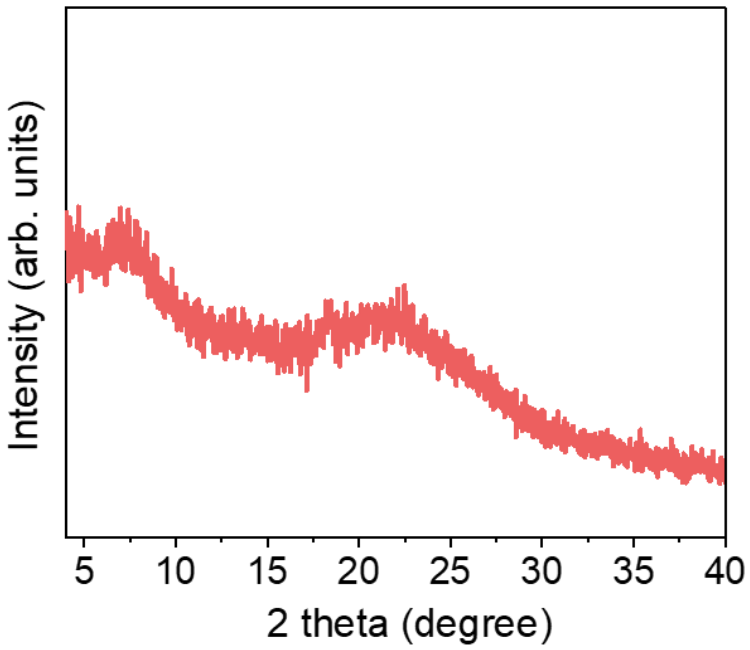

Supplementary Fig. 2 | PXRD pattern of TpTz indicating its largely amorphous nature.

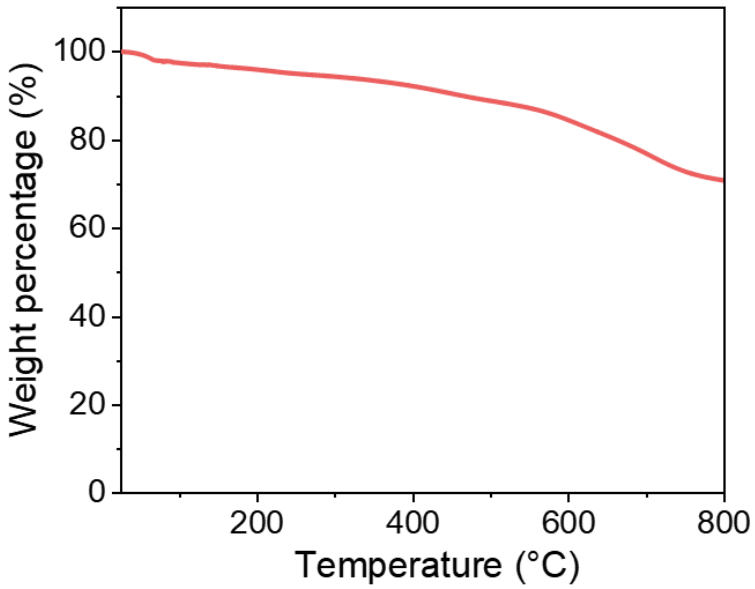

Supplementary Fig. 3 | TGA profile of TpTz from 25 to 800 °C at a heating rate of 10 °C min^{-1} under N_2, indicating its great thermal stability.

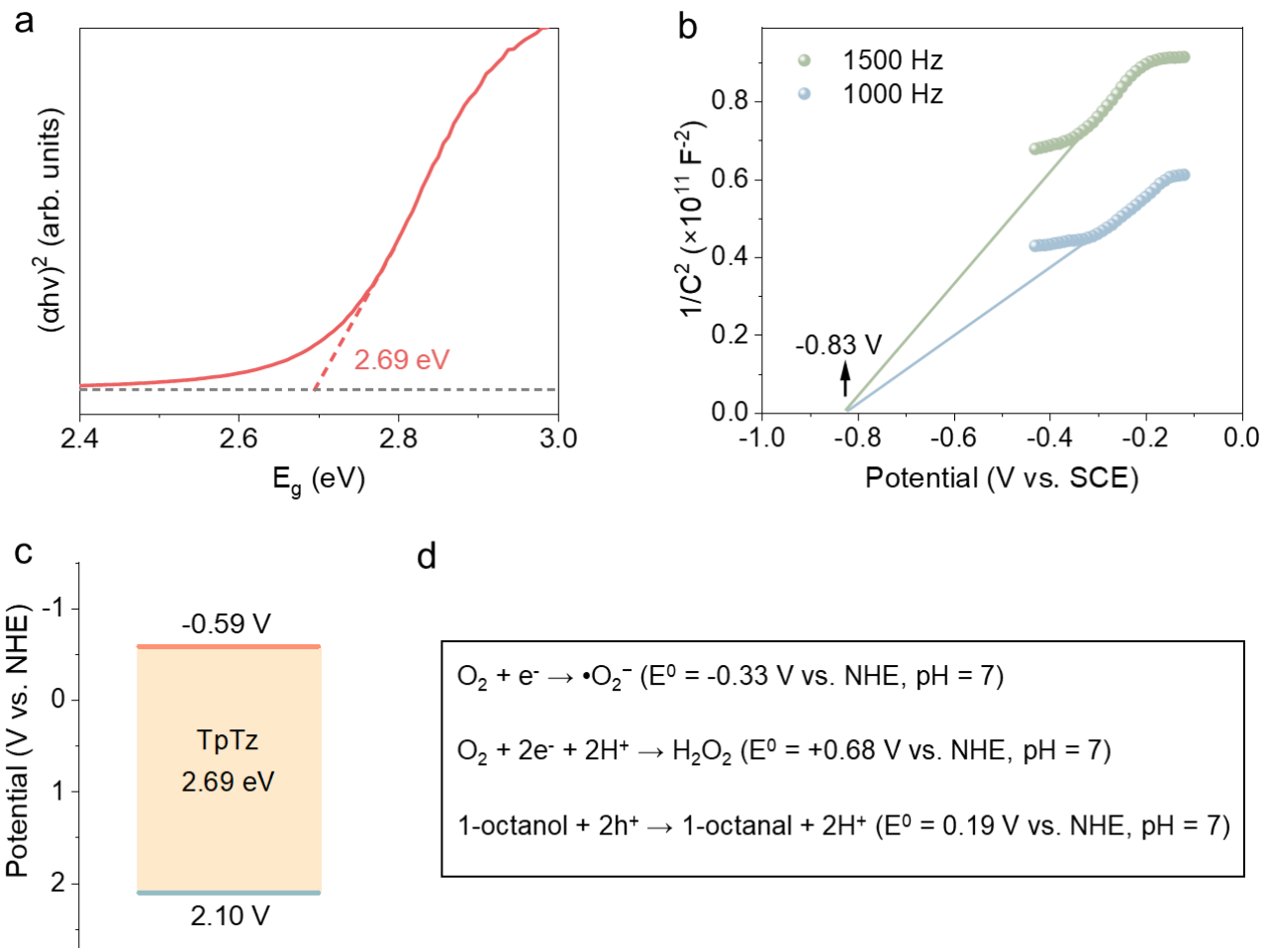

Supplementary Fig. 4 | Optoelectronic properties of TpTz. a, Tauc plot derived from UV-vis diffuse reflectance spectra. **b,** Mott-Schottky plots measured in 0.2 M Na_2SO_4. **c,** Schematic band alignment of TpTz based on the Tauc and Mott-Schottky analyses. **d,** Standard redox potentials of one-electron and two-electron reductions of O_2, and the oxidation of 1-octanol.

The band gap of TpTz was derived from its UV-vis diffuse reflectance spectrum using the Tauc plot method (Supplementary Fig. 4a) (*J. Phys. Chem. Lett.* **2018**, *9*, 6814-6817). To evaluate the conduction band position, Mott-Schottky measurements were performed (Supplementary Fig. 4b). Specifically, 5 mg of TpTz was ultrasonically dispersed in 2 mL of ethanol, and drop-casted onto a fluorine-doped tin oxide (FTO) glass, followed by drying at 80 °C for 2 h. The resulting TpTz-coated FTO was used as the working electrode, with a Pt gauze as the counter electrode, and a saturated calomel electrode (SCE) as the reference electrode. The measurements were conducted in 0.2 M Na_2SO_4 aqueous solution using

a Gamry reference 600 potentiostat under dark at frequencies of 1000 and 1500 Hz. Linear extrapolation of the Mott-Schottky plots yields a flat-band potential of -0.83 V versus SCE, which corresponds to -0.59 V versus normal hydrogen electrode (NHE) according to the equation:

$$E \text{ (vs. NHE)} = E \text{ (vs. SCE)} + 0.241 \text{ V}$$

Assuming the flat-band potential approximates the conduction band minimum, the valence band maximum is calculated to be 2.1 V versus NHE by combining with the optical band gap. This band alignment (Supplementary Fig. 4c) indicates that TpTz possesses sufficient thermodynamic driving force to facilitate both the 2e oxygen reduction reaction and the oxidation of 1-octanol (Supplementary Fig. 4d).

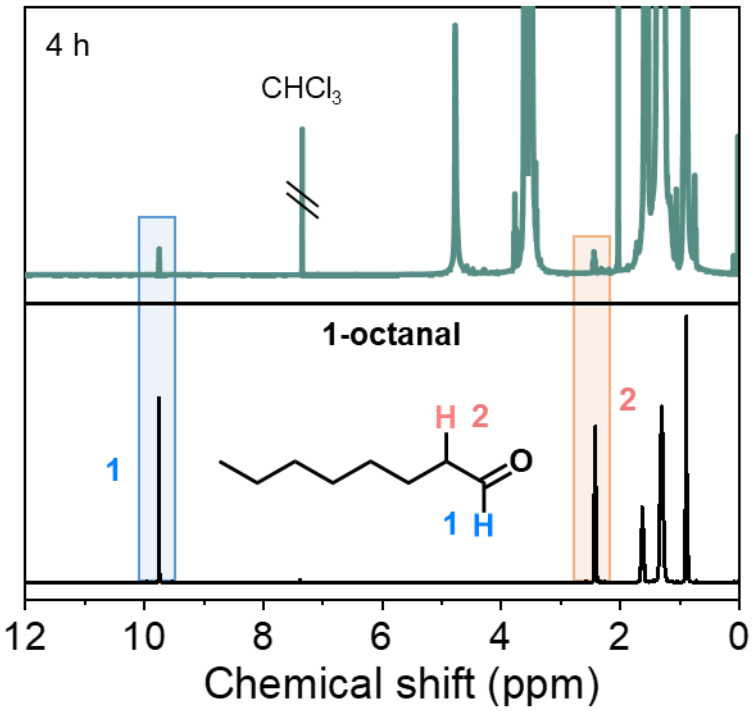

Supplementary Fig. 5 | ^{1}H NMR spectra of (bottom) pure 1-octanal and (top) organic solution after 4 h of irradiation.

The peaks at 9.7 ppm and 2.4 ppm correspond to the aldehyde (-CHO) proton and α-methylene protons adjacent to the carbonyl group of 1-octanal, respectively. Their appearance confirms the photocatalytic oxidation of 1-octanol to 1-octanal. The absence of the characteristic signal for 1-octanoic acid at 11.5 ppm indicates no further oxidation of 1-octanal.

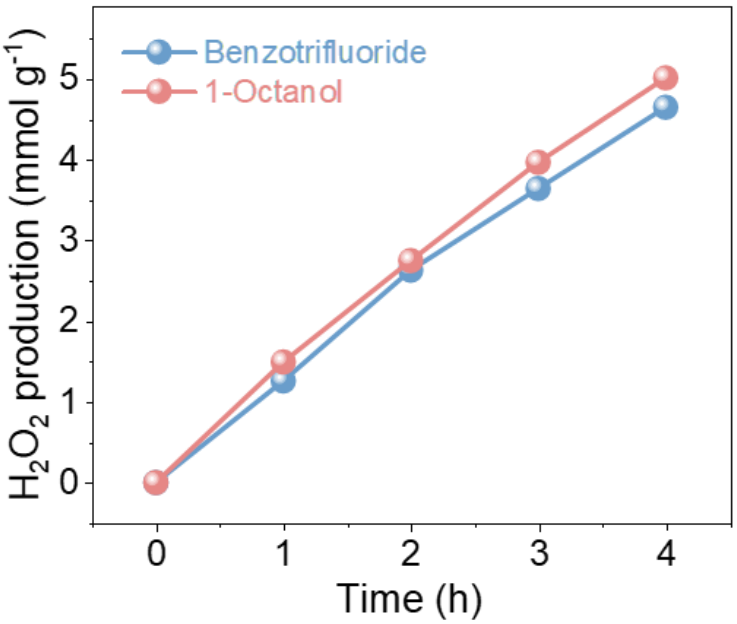

Supplementary Fig. 6 | Photocatalytic H_2O_2 production in biphasic systems with 1-octanol and benzotrifluoride (with 10 vol% 1-octanol) as the organic phase.

To evaluate whether O_2 availability limits the reaction, benzotrifluoride with higher O_2 solubility (18 mmol L^{-1}) was used to replace 1-octanol (9.5 mmol L^{-1}) as the organic phase (*J. Chem. Educ.* **1996**, *73*, 143; *J. Chem. Thermodynamics*, **1978**, 10, 817-822), while maintaining 10 vol% 1-octanol as the sacrificial electron donor. As shown above, no appreciable enhancement in H_2O_2 production was observed compared with the 1-octanol system. This result indicates that further increasing O_2 availability does not further improve the catalytic activity or stability of the photocatalyst, suggesting that O_2 mass transport is not the limiting factor in the present reaction system.

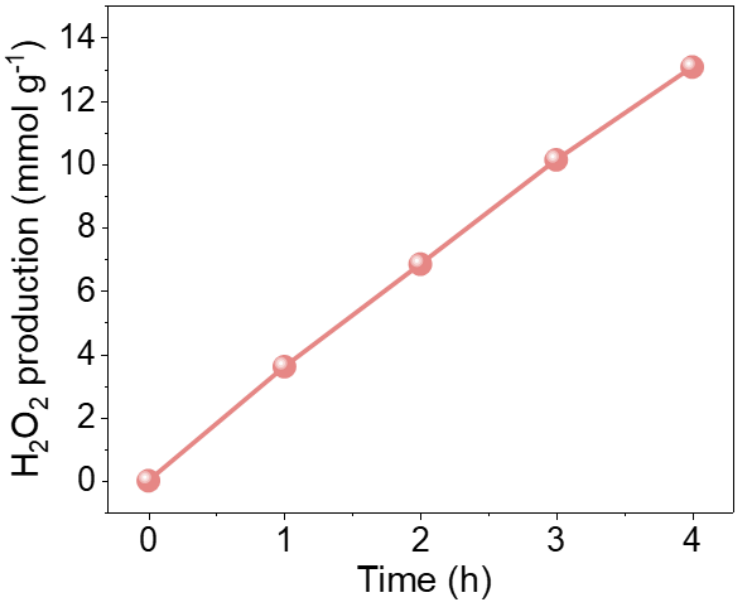

Supplementary Fig. 7 | Photocatalytic H_2O_2 production on TpTz at 80 °C in the biphasic system under visible light irradiation (λ >420 nm, 300 mW/cm^2)

To evaluate the photocatalytic performance of TpTz under recycling conditions, we conducted photocatalytic H_2O_2 production at 80 °C with otherwise identical conditions. As displayed in Supplementary Fig. 7, TpTz exhibits a continuous and nearly linear H_2O_2 accumulation over 4 h of irradiation, reaching a total yield of 13.1 mmol g^{-1} and a final concentration of 27 mM, approximately 2.7 times higher than that at room temperature. This improvement can be attributed to accelerated reaction kinetics and reduced activation barriers at higher temperature, which facilitate both charge transfer and surface redox processes (*ACS Catal.* **2024**, 14, 16543-16550; *Nano Research*, **2026**, 19, 94908130).

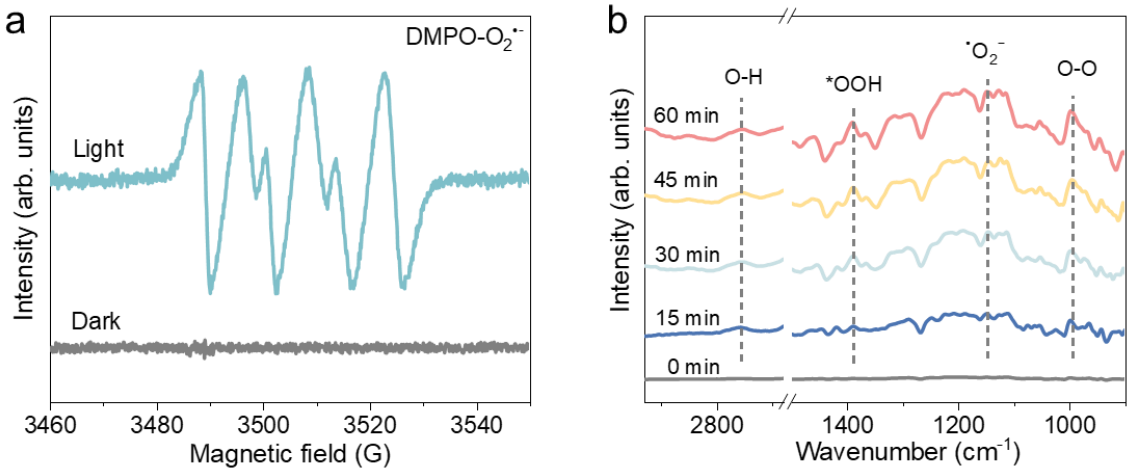

Supplementary Fig. 8 | Mechanistic studies on H_2O_2 production. a, EPR spectra of DMPO-$^{\bullet}O_2^-$ adducts recorded in the dark and under visible-light irradiation (λ > 420 nm) using TpTz as the photocatalyst in an O_2 atmosphere. **b,** *Operando* DRIFT spectra of TpTz collected under visible-light illumination at different time intervals.

To identify potential intermediates, EPR spectroscopy was performed using 5,5-dimethyl-pyrroline N-oxide (DMPO) as a spin-trapping reagent. As shown in Supplementary Fig. 8a, characteristic signals assignable to the DMPO-$^{\bullet}O_2^-$ adduct are observed on TpTz under visible-light irradiation, confirming the generation of $^{\bullet}O_2^-$ upon illumination (*Adv. Funct. Mater.* **2023**, *33*, 2302964; *Nat. Commun.* **2023**, *14*, 5238).

Moreover, *operando* DRIFTS measurements were conducted using a Thermo Fisher IS50 spectrometer. Before the measurement, the TpTz sample (10 mg) was degassed under vacuum at 120 °C for 2 h. The sample was then loaded into a custom-built IR reaction chamber, purged with Ar for 1 h, followed by exposure to H_2O-saturated O_2 for 30 min to establish adsorption equilibrium. A background spectrum was recorded in the dark. Subsequently, the sample was irradiated under visible light (λ > 420 nm), and DRIFTS spectra were collected at designated time intervals. Each spectrum was acquired by averaging 64 scans at a resolution of 4 cm^{-1}.

As shown in Supplementary Fig. 8b, a gradually increasing signal at 1147 cm^{-1} is attributed to the formation of the $^{\bullet}O_2^-$ intermediate, while the band at 1390 cm^{-1} corresponds to the *OOH species

(*Angew. Chem. Int. Ed.* **2024**, *63*, e202404563; *Angew. Chem. Int. Ed.* **2024**, *63*, e202404077). The characteristic stretching vibrations of the O-O bond (995 cm^{-1}) and O-H bond (2761 cm^{-1}) in H_2O_2 were also observed, with intensities progressively increasing upon irradiation (*Adv. Mater.* **2023**, *35*, 2210110; *Angew. Chem. Int. Ed.* **2023**, *62*, e202310556). These results, together with the EPR analysis, indicate that H_2O_2 photogeneration mainly follows a two-step single-electron transfer pathway.

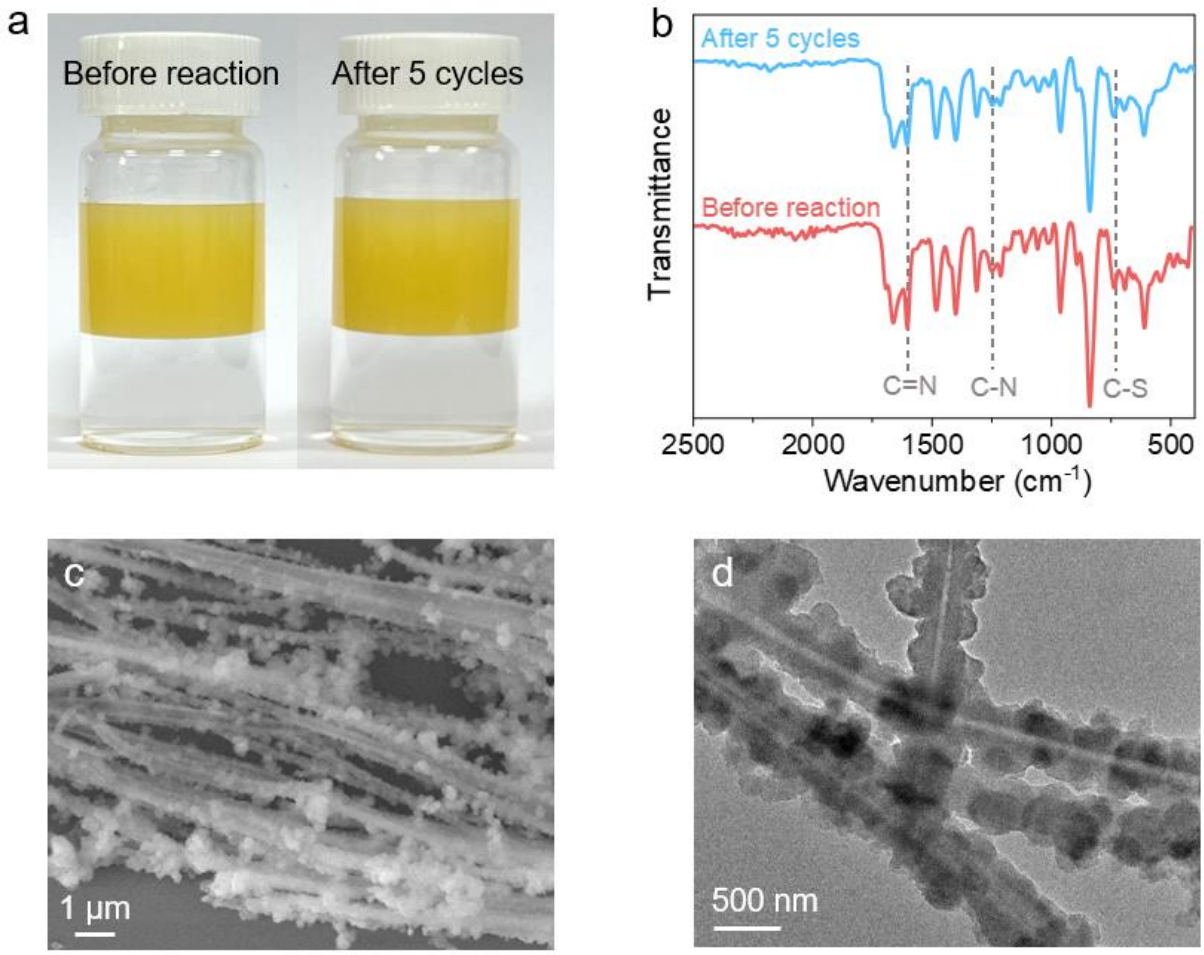

Supplementary Fig. 9 | Characterizations of recovered TpTz after cycling experiments. a, Photographs and **b,** FT-IR spectra of TpTz before and after five photocatalytic cycles, showing retention of structural features. **c,** SEM and **d,** TEM images of TpTz after the recycling test, indicating preserved morphology and microstructure.

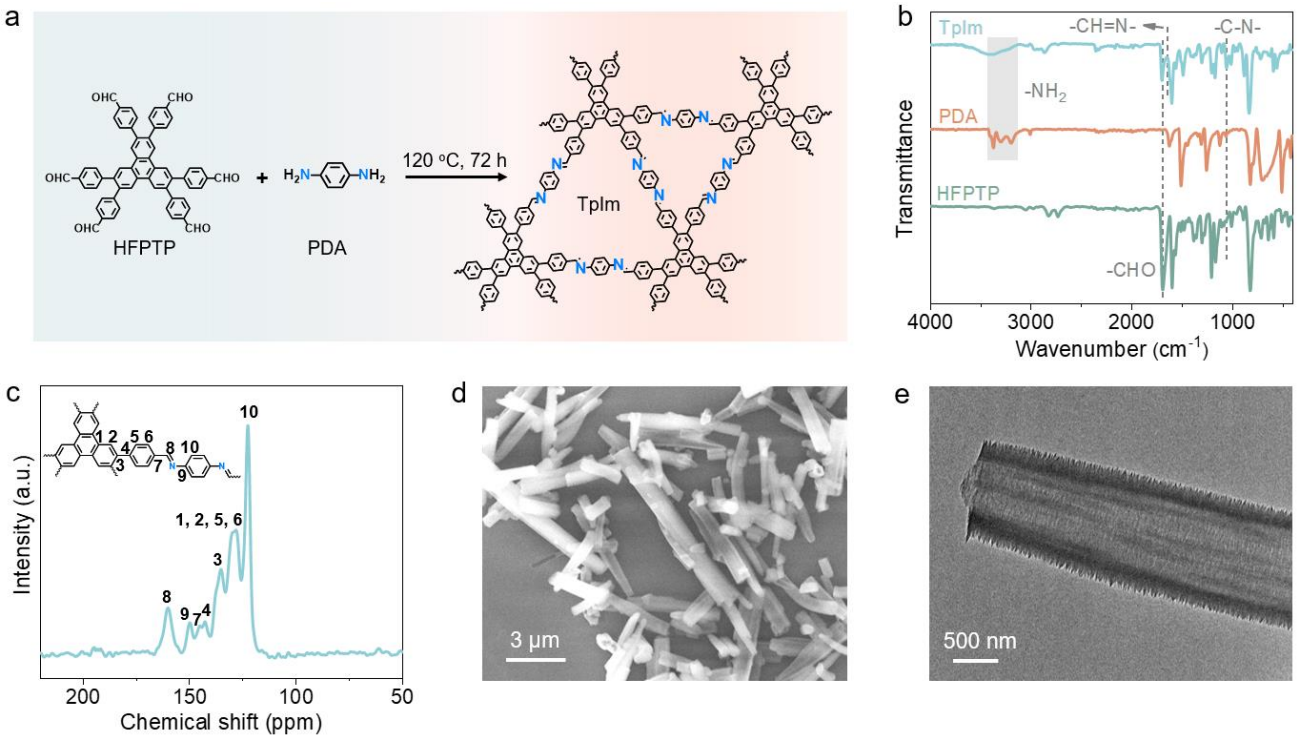

Supplementary Fig. 10 | Synthesis and characterizations of TpIm. a, FT-IR spectra of TpIm and its corresponding monomer precursors, **b,** solid-state ^{13}C NMR spectrum, **c,** SEM image and **d,** TEM image of TpIm.

TpIm was synthesized via a polycondensation reaction between HFPTP and PDA, following a previously reported procedure with slight modifications (Supplementary Fig. 10a) (*Angew. Chem. Int. Ed.* **2019**, *58*, 15922-15927). Typically, HFPTP (80 mg, 0.09 mmol) and PDA (30 mg, 0.27 mmol) were ultrasonically dispersed in a solvent mixture of *o*-DCB, *n*-BuOH, and 6 M acetic acid (4.4 mL, 5/5/1, v/v/v) in a 25 mL Pyrex tube. The tube was degassed by three vacuum-argon filling cycles, sealed under vacuum, and heated at 120 °C for 72 h. After cooling to room temperature, the precipitate was collected by centrifugation, thoroughly washed with DMF, THF, and acetone, and finally dried under vacuum at 80 °C overnight to afford TpIm as a light-yellow powder (yield: 92%).

As shown in Supplementary Fig. 10b, FT-IR spectroscopy provides key evidence for the successful polymerization of the monomers into imine (-CH=N-)-linked TpIm. The characteristic vibrational bands of N-H (3300 cm^{-1}) and C=O (1690 cm^{-2}) from the unreacted monomers are significantly

attenuated. Simultaneously, a new absorption band emerges at 1622 cm^{-1}, which is attributed to the imine linkages formed in the TpIm framework. Solid-state ^{13}C NMR spectrum further supports this structural assignment, showing a distinct resonance at 169 ppm, characteristic of the imine carbon atoms (Supplementary Fig. 10c). In addition, SEM and TEM images reveal that TpIm adopts a hollow nanotubular morphology, similar to that observed for TpTz (Supplementary Fig. 10d,e).

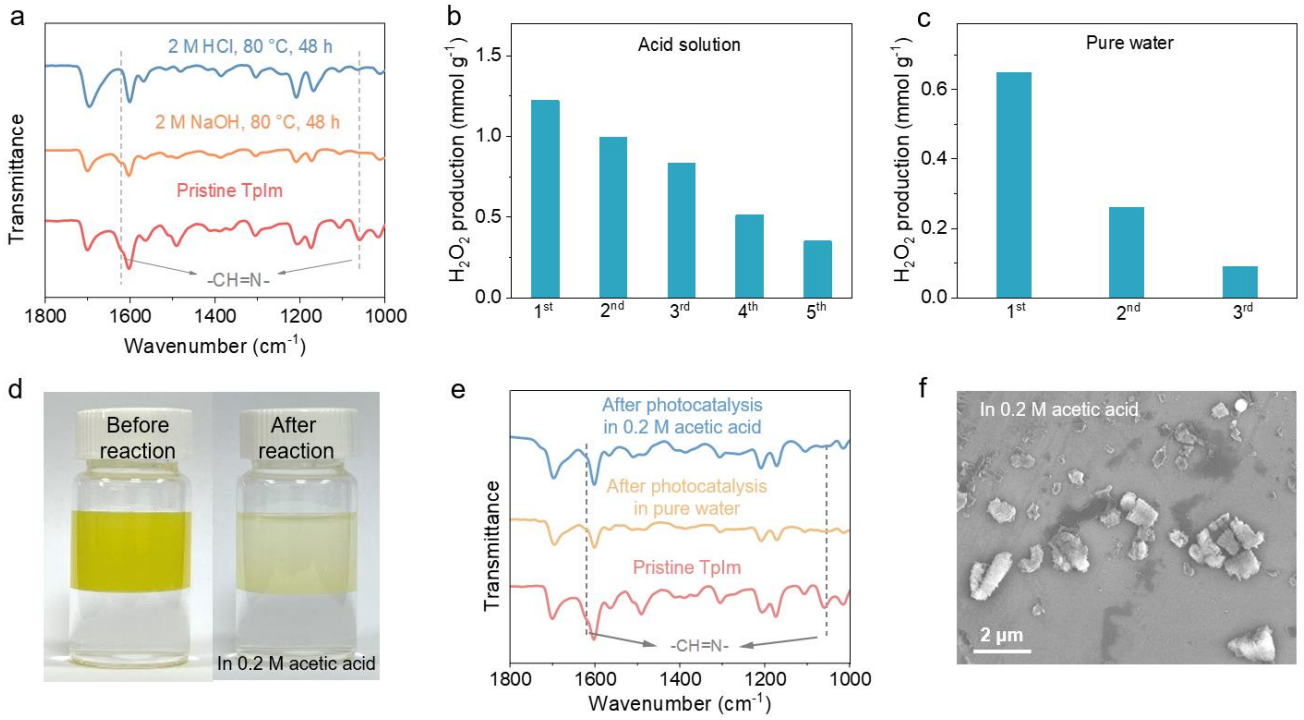

Supplementary Fig. 11 | Stability of TpIm. a, FT-IR spectra of TpIm before and after treatment in 2 M HCl and 2 M NaOH at 80 °C for 48 h. **b,** Photocatalytic cycling tests for H_2O_2 production in a biphasic system with 0.2 M acetic acid as the aqueous phase. **c,** Photocatalytic cycling tests for H_2O_2 production in a biphasic system with pure water as the aqueous phase. **d,** Photographs showing of TpIm before and after the cycling test . **e,** FT-IR spectra of TpIm before and after the cycling test. **f,** SEM image of TpIm after the cycling experiment.

The durability of TpIm was evaluated under harsh chemical environments and repeated photocatalytic cycling. FT-IR spectra of TpIm samples recovered after treatment in 2 M HCl and 2 M NaOH at 80 °C for 48 h exhibit a marked decrease in the characteristic imine stretching band at ~1620 cm^{-1} (Supplementary Fig. 11a), indicating partial cleavage of imine linkages and loss of structural integrity under extreme pH conditions. Photocatalytic cycling experiments reveal a pronounced decline in catalytic performance in both acidic and neutral aqueous media, accompanied by visible mass loss and increased transparency of the photocatalyst dispersion (Supplemental Fig. 11b-d). FT-IR spectra of samples recovered after cycling show complete disappearance of the –CH=N– vibrational signature (Supplemental Fig. 11e). SEM imaging further reveals significant morphological degradation,

confirming structural collapse under prolong photocatalysis (Supplemental Fig. 11f). These results demonstrate severe molecular and morphological instability from the combined effects of reactive oxygen species (ROS)-mediated oxidation and acid-catalyzed hydrolysis.

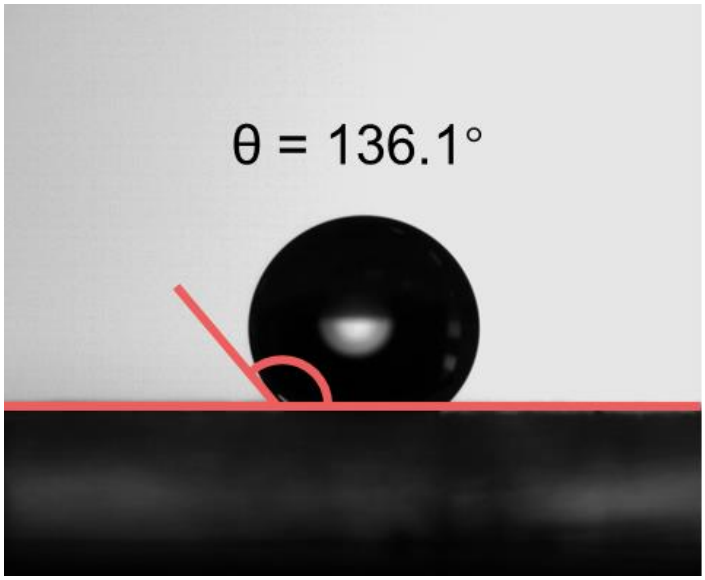

Supplementary Fig. 12 | Water contact angle of TpTz.

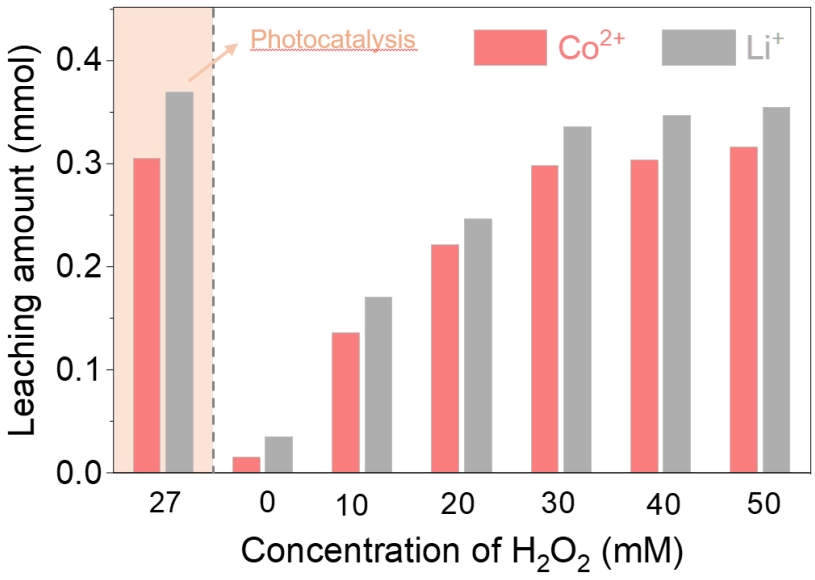

Supplementary Fig. 13 | Comparison of $LiCoO_2$ leaching performance between *in-situ* photogenerated H_2O_2 versus direct addition of commercial H_2O_2 solution with varying concentrations (0-50 mM).

To directly verify the role of H_2O_2 in enabling $LiCoO_2$ leaching, additional experiments were conducted through directly adding comparable commercial H_2O_2 to the recycling system. To simulate photocatalytic conditions, a biphasic configuration was maintained using a 1:1 ratio of 1-octanol (oil phase) and 0.2 M acetic acid (aqueous phase with 50 mg $LiCoO_2$). Considering the gradual accumulation of photogenerated H_2O_2, varying H_2O_2 concentrations (0 - 50 mM) were prepared from a 30 wt% stock and added to the reaction mixture at 80°C. Our results indicate that the leaching amount increases progressively with H_2O_2 concentration up to 30 mM, confirming that H_2O_2 availability is essential for triggering $LiCoO_2$ leaching under mild acidic conditions. Moreover, metal leaching concentrations at 30 mM H_2O_2 is similar to that achieved in photocatalytic system. When H_2O_2 concentration exceeds 30 mM, the leaching efficiency reaches a plateau, likely due to the accelerated decomposition of H_2O_2 induced by released Co^{2+}. Notably, this 30 mM threshold aligns well with the photocatalytic H_2O_2 yield over 4 h at 80°C. This result demonstrates that the photocatalytic system can continuously provide a sufficient amount of H_2O_2 to achieve the maximum leaching efficiency observed in the control experiments.

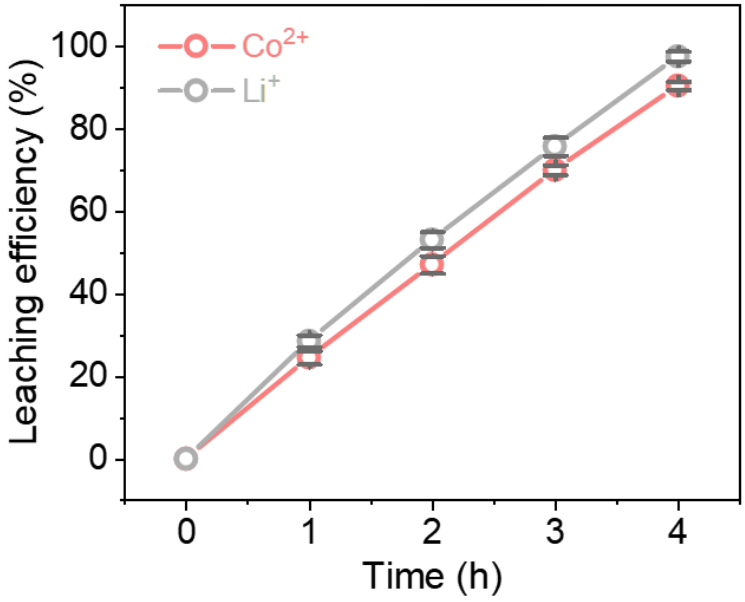

Supplementary Fig. 14 | Time-dependent metal leaching efficiencies from 20 mg of $LiCoO_2$, with error bars representing the standard deviation of n = 3 independent replicates.

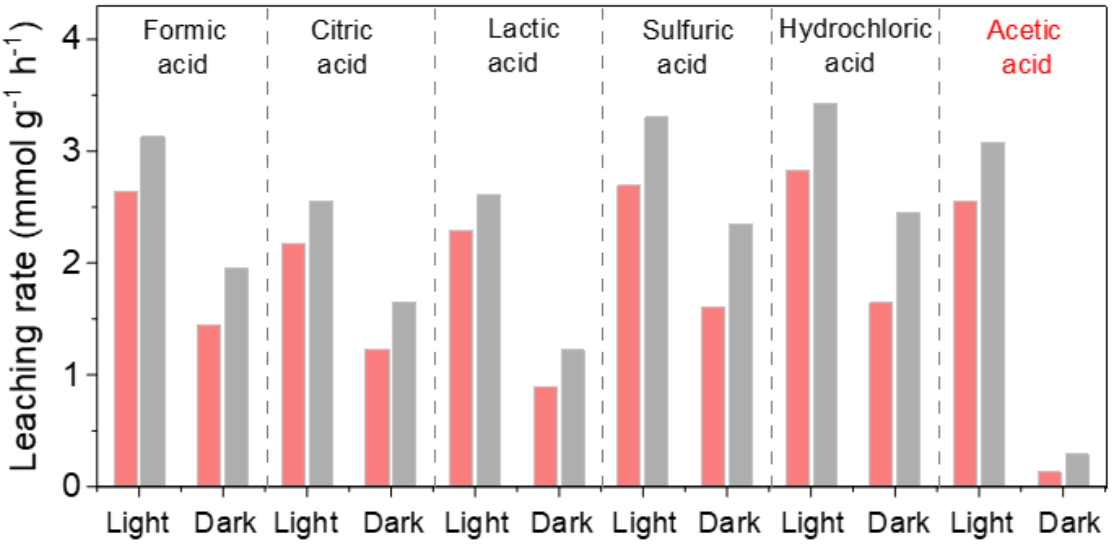

Supplementary Fig. 15 | Metal leaching rates in different acidic solutions (0.2 M) over TpTz under light and dark conditions in a 1-octanol/H_2O biphasic system under O_2 atmosphere.

We evaluated several acids, including formic, citric, lactic, sulfuric, and hydrochloric acids, to assess their influence on leaching performance in our photocatalytic system. All experiments were conducted using 0.2 M of each acid under otherwise identical conditions to those used for acetic acid. As summarized, all tested acids exhibit comparable metal leaching rates of approximately 3 mmol g^{-1} h^{-1} under visible light irradiation; however, significant differences are observed under dark conditions, where no H_2O_2 is produced. Specifically, all acids except acetic acid demonstrate notable leaching activity in the dark, likely due to their strong acidity or reducing nature (*Energy Environ. Sci.* **2022**, *15*, 2732). These background effects inevitably obscure the specific role of H_2O_2 in the leaching process. In contrast, acetic acid provides negligible dark leaching, enabling the observed activity to be primarily attributed to *in-situ* photogenerated H_2O_2. Consequently, acetic acid was selected as the optimal medium, as it allows for clear assessment of H_2O_2-mediated leaching while offering distinct advantages in terms of operational safety, sustainability, and cost-effectiveness.

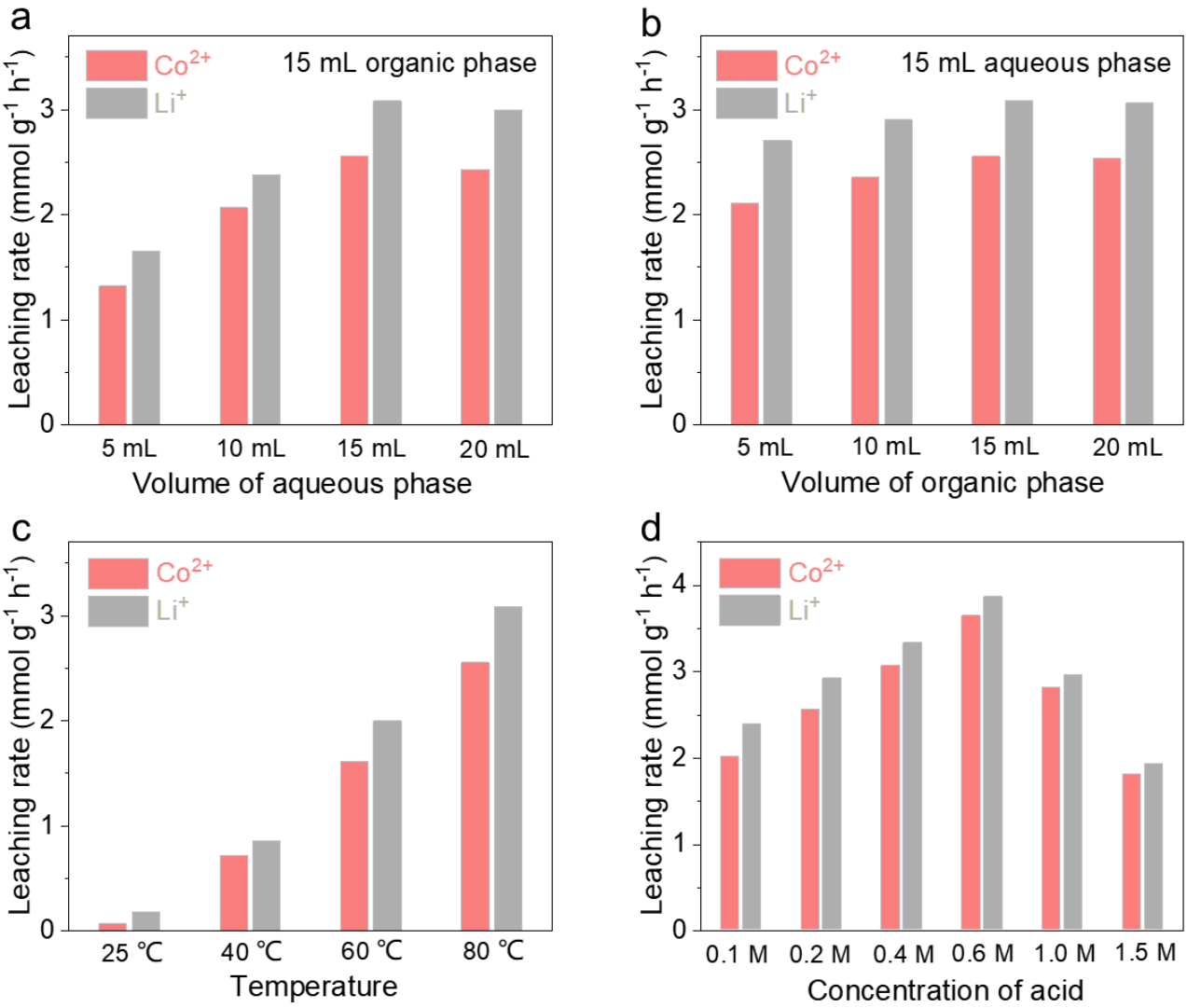

Supplementary Fig. 16 | Effects of various reaction parameters on the metal leaching rate using TpTz as the photocatalyst. a, Influence of organic phase volume. **b**. Influence of aqueous phase volume. **c,** Influence of reaction temperature. **d,** Influence of acetic acid concentration in the aqueous phase.

We systematically investigated the influence of several key reaction parameters on the metal leaching rate. First, the water-to-oil volume ratio plays a critical role in determining the leaching efficiency. The optimal performance is observed at a 1:1 ratio (Supplementary Fig. 16a,b), which is believed to provide a balanced environment where light can effectively penetrate the organic phase to drive H_2O_2 production, while maintaining sufficient H_2O_2 concentration in the aqueous phase to support metal leaching. Second, the reaction temperature significantly affects the leaching rates. Increasing the

temperature from 25 to 80 °C leads to a dramatic enhancement in metal leaching, with Li^+ and Co^{2+} showing approximately 35-fold and 17-fold increases, respectively (Supplementary Fig. 16c). This improvement is likely attributed to thermally accelerated photocatalytic activity, which enhances both H_2O_2 generation and the reductive dissolution of Co^{3+} species in $LiCoO_2$. Based on this, 80 °C is selected as the optimal operating temperature, balancing improved reaction kinetics with practical considerations, since higher temperatures would require pressurized vessels to prevent solvent evaporation due to water boiling. Lastly, the concentration of acetic acid in the aqueous phase exhibits a volcano-shaped dependence on the metal leaching rates (Supplementary Fig. 16d). The maximum extraction performance is achieved at 0.6 M acetic acid, with leaching rates reaching 3.9 mmol h^{-1} g^{-1} for Li^+ and 3.6 mmol h^{-1} g^{-1} for Co^{2+}. This trend is primarily attributed to the influence of proton availability on the photocatalytic oxygen reduction reaction (ORR). Moderate acid concentrations enhance proton-coupled electron transfer during ORR, thus facilitating efficient H_2O_2 production and subsequent metal leaching. However, beyond the optimal point, excessive proton accumulation near the photocatalyst–solution interface likely introduces a kinetic barrier to electron transfer, suppressing ORR activity and reducing H_2O_2 formation (*Nat. Energy* **2023**, *8*, 1137-1144).

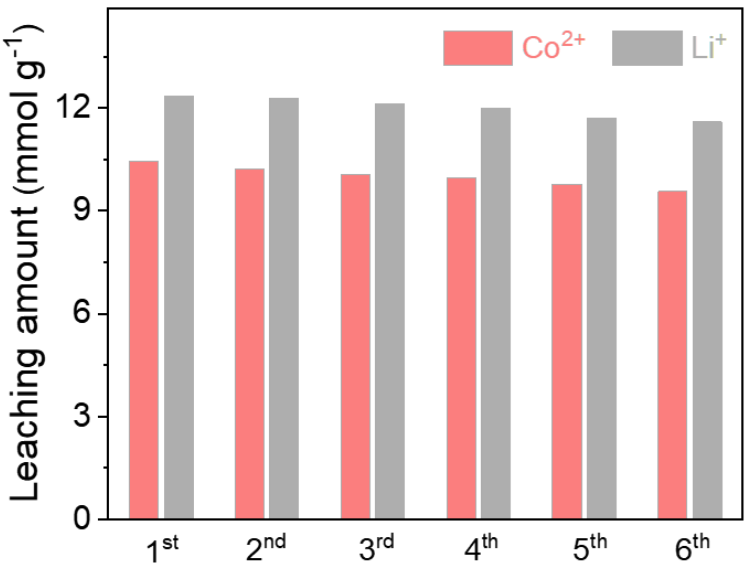

Supplementary Fig. 17 | Cycling performance of TpTz in the photocatalytic leaching of metals from 50 mg of $LiCoO_2$ for each cycle.

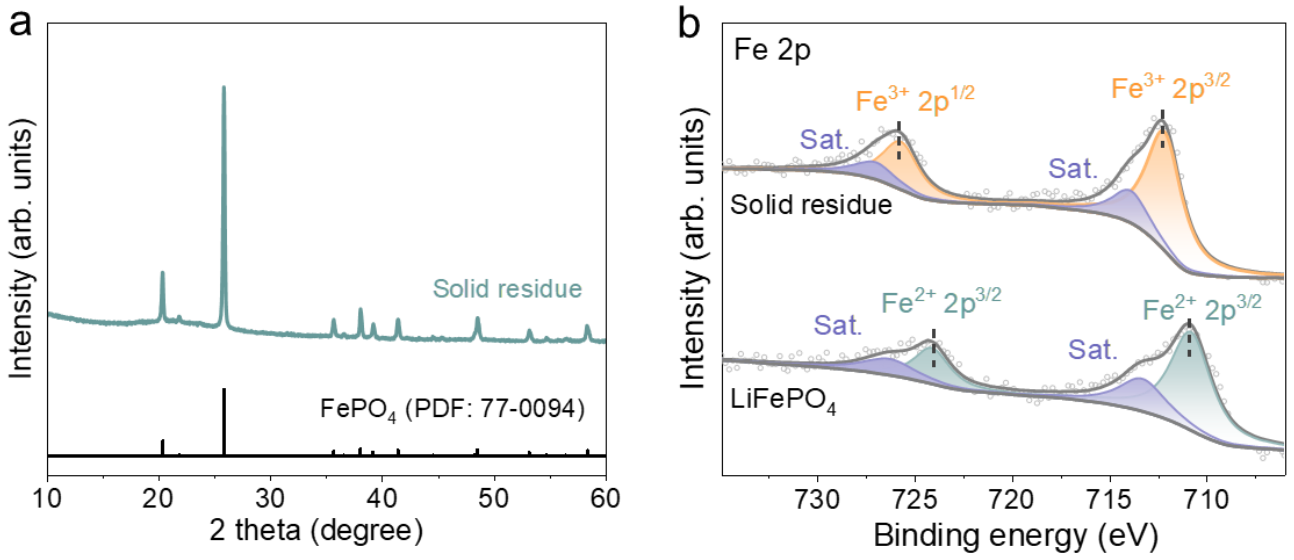

Supplementary Fig. 18 | a, XRD pattern of solid residue collected after photocatalytic recycling of Li^+. **b,** Fe 2p XPS spectra of $LiFePO_4$ and solid residue.

The residues collected after photocatalytic recycling of Li^+ were thoroughly washed with deionized water, and dried prior to characterization. The XRD pattern of the solid residue shows characteristic diffraction peaks consistent with the standard reference pattern of $FePO_4$. In addition, the Fe 2p XPS spectrum of pristine $LiFePO_4$ exhibits two characteristic peaks at 725.8 eV (Fe $2p^{3/2}$) and 712.3 eV (Fe $2p^{1/2}$), corresponding to the Fe^{2+} state. In contrast, the Fe 2p XPS spectrum of the residue shows a clear shift to higher binding energies, with peaks at 723.8 eV and 710.7 eV, respectively, indicating oxidation to the Fe^{3+} state.

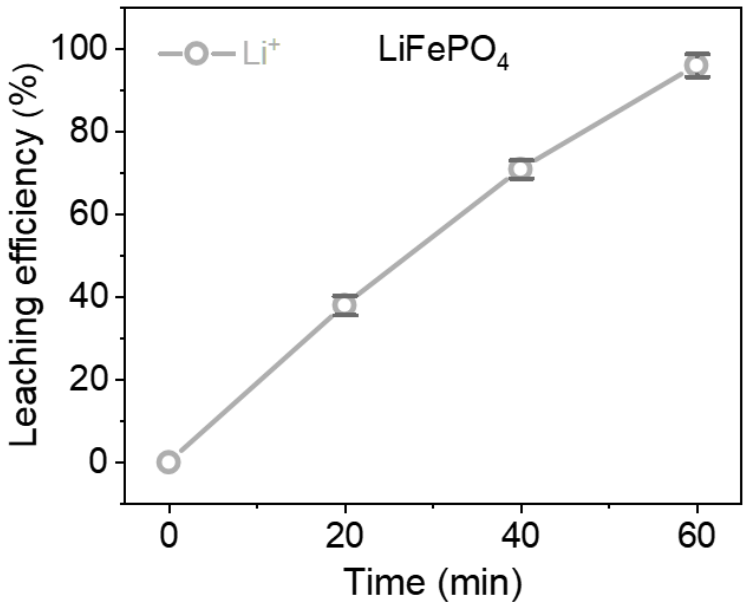

Supplementary Fig. 19 | Time-dependent metal leaching efficiencies from 50 mg of $LiFePO_4$.

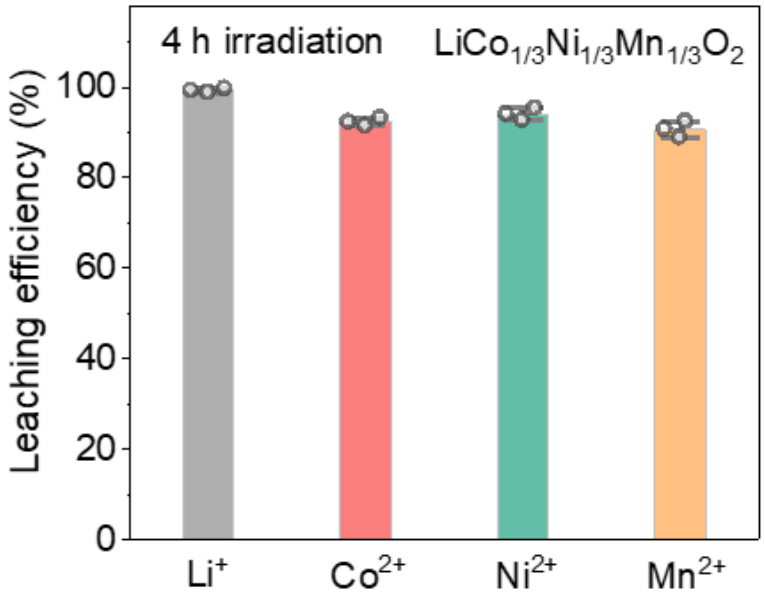

Supplementary Fig. 20 | Time-dependent metal leaching efficiencies from 20 mg of $LiCo_{1/3}Ni_{1/3}Mn_{1/3}O_2$ after 4 h irradiation. The values of bar chart are means of n= 3 independent replicates, with error bars representing the standard deviation of three replicates.

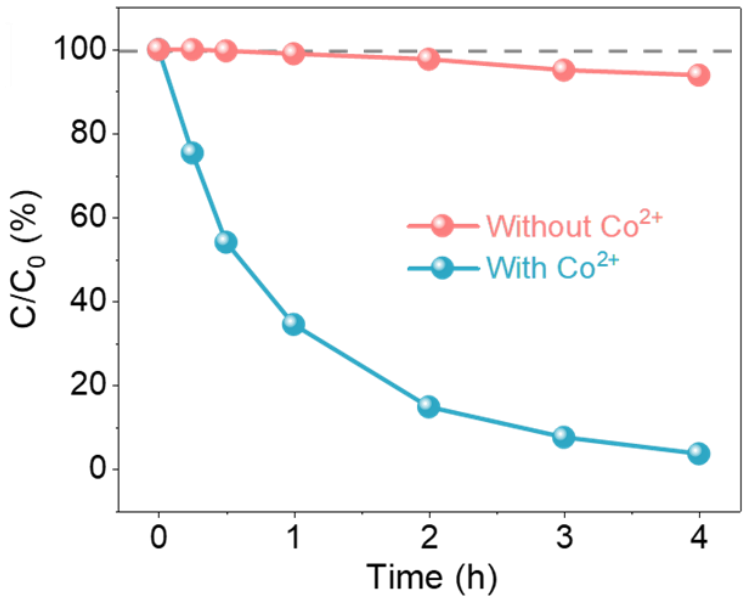

Supplementary Fig. 21 | H_2O_2 decomposition with and without Co^{2+} under conditions mimicking the leaching environment.

To investigate the effect of Co^{2+} on H_2O_2 stability in the photocatalytic system, control experiments were conducted under conditions representative of the leaching environment. A biphasic reaction consisting of an aqueous phase (15 mL) containing 30 mM H_2O_2 and 20 mM cobalt acetate, together with 15 mL of 1-octanol as the organic phase, was prepared in the absence of photocatalyst. These concentrations are comparable to those reached during the 4 h photocatalytic recycling reaction. For comparison, a Co^{2+}-free control was prepared under otherwise identical conditions without cobalt acetate. Both systems were maintained at 80 °C under visible-light irradiation ($\lambda > 420$ nm, 300 mW cm^{-2}), and the H_2O_2 concentration in the aqueous phase was monitored over time. As shown above, in the absence of Co^{2+}, H_2O_2 remains highly stable, with negligible decomposition (< 10%) over 4 h. In contrast, in the presence of Co^{2+}, fast H_2O_2 decomposition occurs, with approximately 50% of the initial H_2O_2 consumed within the first 30 min, and nearly complete decomposition after 4 h. These results demonstrate that Co^{2+} strongly promotes H_2O_2 decomposition, supporting the conclusion that accumulated Co^{2+} accelerates this process during leaching.

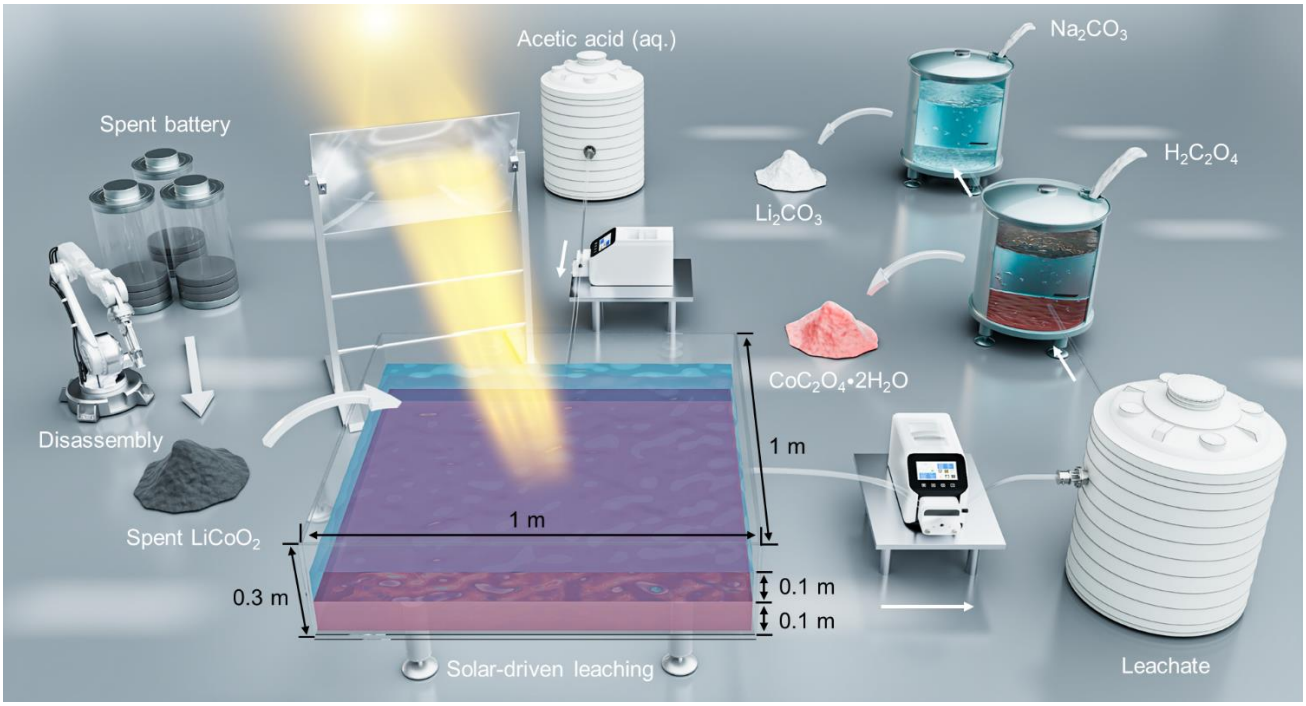

Supplementary Fig. 22 | Proposed scaled-up reactor configuration used for the technoeconomic analysis discussed in the main text.

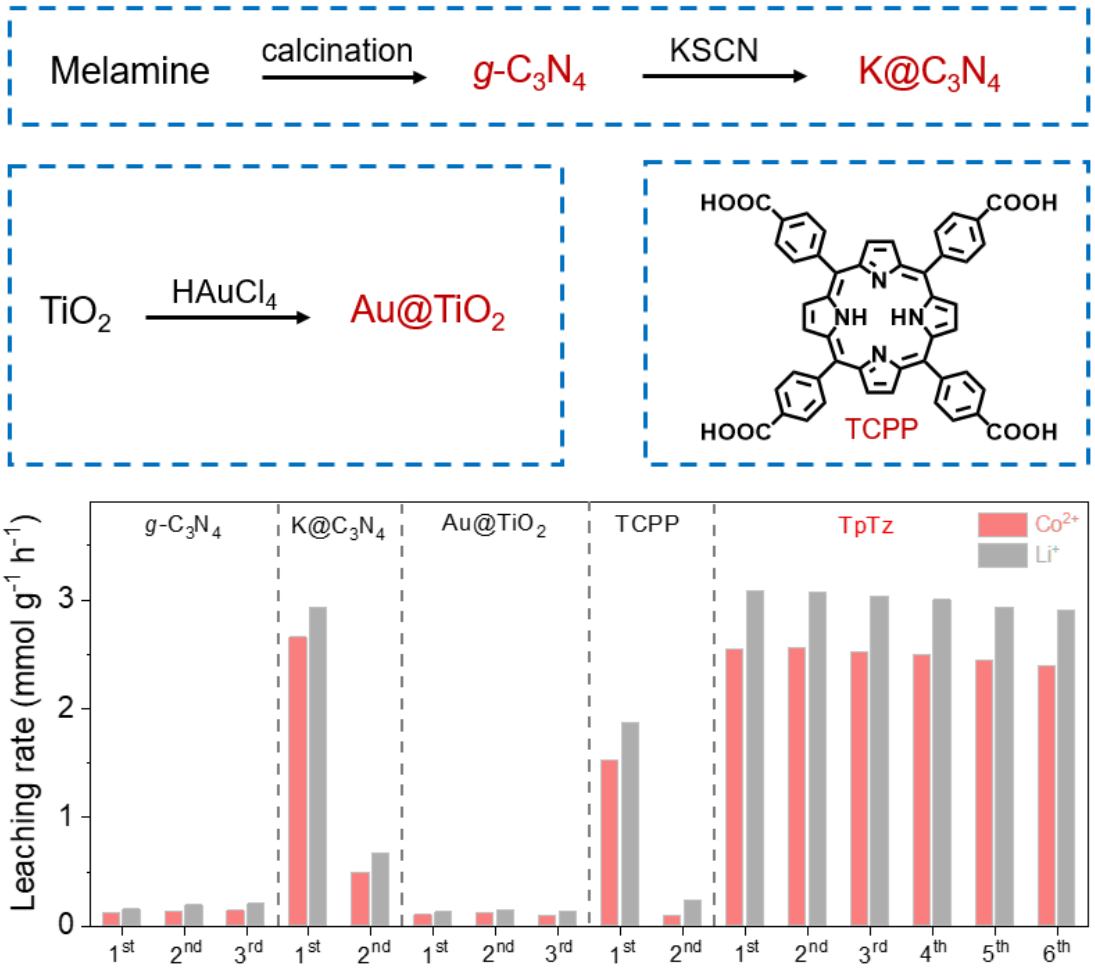

Supplementary Fig. 23 | Comparison of leaching rate and stability of *g*-C_3N_4, K@C_3N_4, TCPP, and TpTz under identical conditions.

The photocatalysts involved in this study were synthesized according to previously reported procedures. Specifically, pristine *g*-C_3N_4 was prepared by direct thermal polymerization of melamine at 550 °C for 4 h under an argon atmosphere (*Adv. Funct. Mater.* **2022**, 32, 2205119). Potassium doped *g*-C_3N_4 (K@C_3N_4) was synthesized by grinding 2 g of pristine *g*-C_3N_4 with 1 g of KSCN, followed by annealing at 500 °C for 5 h under argon (*Adv. Funct. Mater.* **2022**, 32, 2205119). Gold nanoparticle modified TiO_2 (Au@TiO_2) was fabricated via a deposition-precipitation method. $HAuCl_4$ (40 mg) and TiO_2 (1.0 g) were stirred in deionized water at 65 °C. The pH was adjusted to 6-7 using 0.05 M NaOH aqueous solution and stirred for an additional 1 h (*Angew. Chem. Int. Ed.* **2021**, 60, 12074-12081). tetra(4-carboxyphenyl) porphyrin (TCPP) photocatalyst was synthesized through a pH-controlled self-

assembly process (*Nat. Energy* **2023**, 8, 361-371), in which a TCPP aqueous solution in 0.5 M KOH was acidified to pH 4 with 0.1 M HCl, and stirred at 80 °C for 72 h. As shown above, although pristine *g*-C_3N_4 exhibits good stability, its photocatalytic H_2O_2 production activity is significantly lower than that of TpTz, resulting in negligible Co^{2+} and Li^+ recovery rates. Chemical modification through potassium doping improves the activity of *g*-C_3N_4 to some extent, but at the expense of durability, leading to noticeable degradation during reaction. Other tested alternatives, including TCPP and Au@TiO_2, do not satisfy either the performance benchmarks or the required stability criteria. Based on the present results, TpTz remains the optimal choice as it provides the best balance of catalytic efficiency, structural robustness, and overall leaching performance.

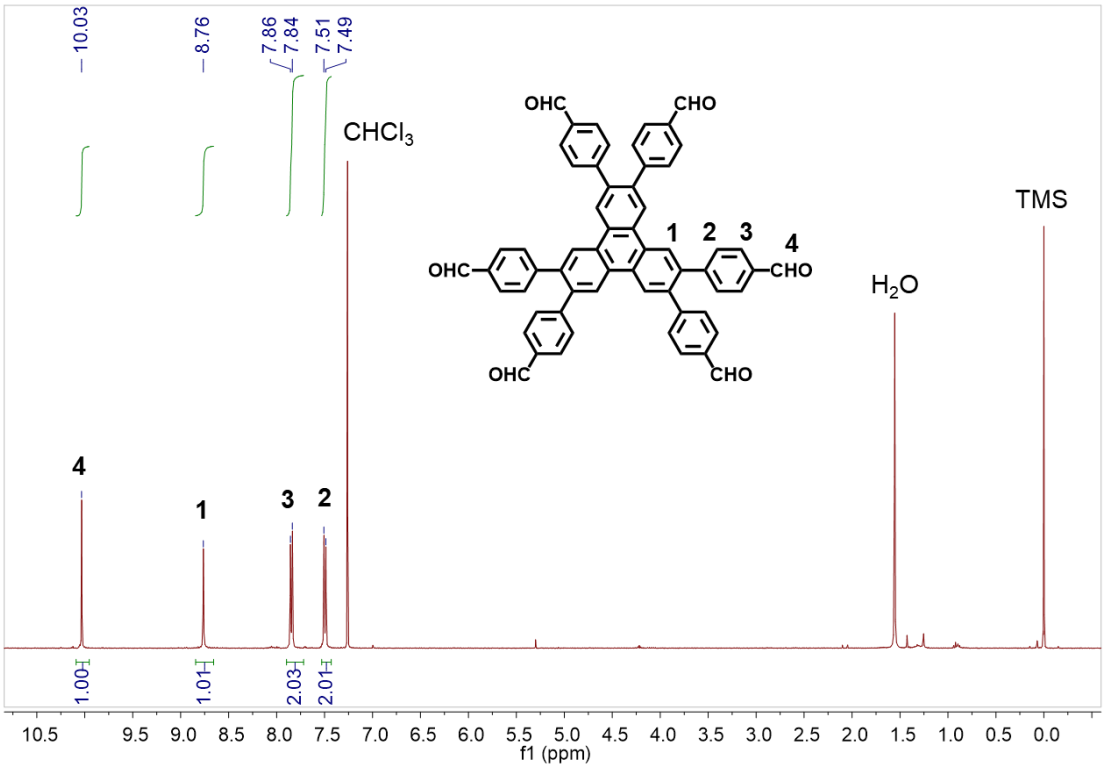

Supplementary Fig. 24 | ^{1}H NMR spectrum of HFPTP (400 MHz, $CDCl_3$, at 298 K).

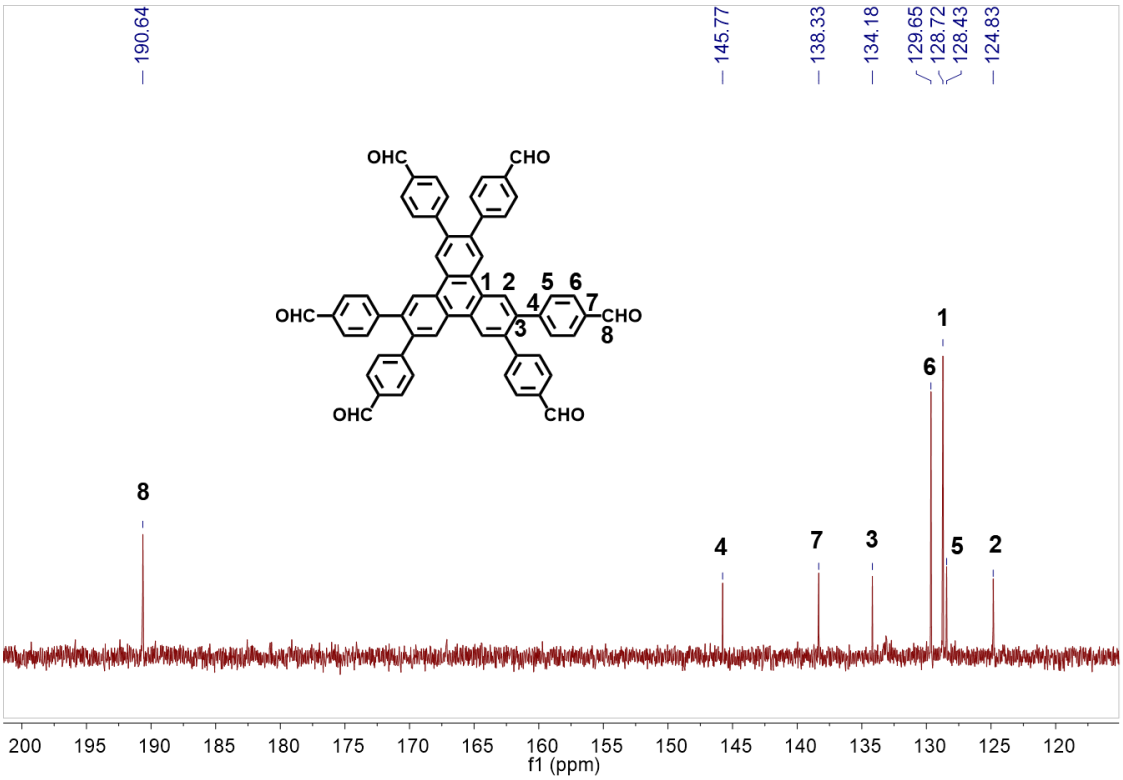

Supplementary Fig. 25 | ^{13}C NMR spectrum of HFPTP (400 MHz, $CDCl_3$, at 298 K).

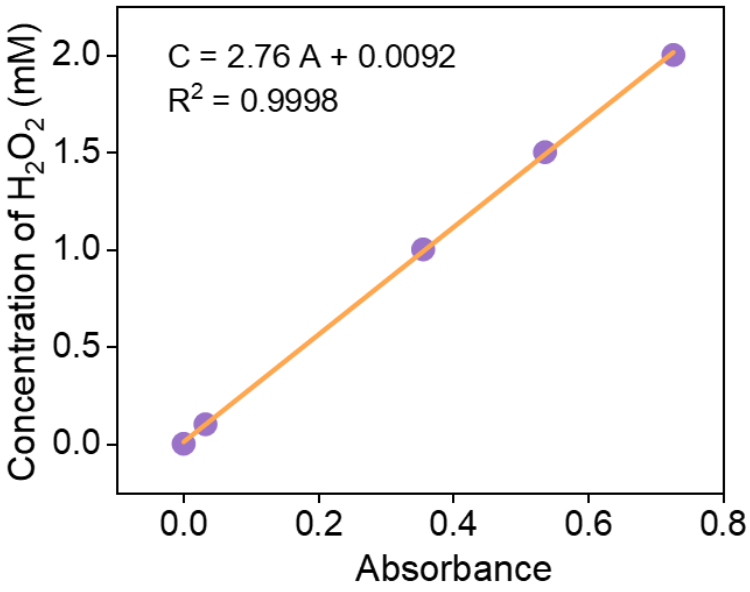

Supplementary Fig. 26 | Calibration curve of the xylenol orange/Fe^{2+} colorimetric assay, showing the linear relationship between H_2O_2 concentration and absorbance at 580 nm.

Supplementary Table 1 | A quantitative comparison of energy consumption, chemical usage, and carbon emissions among pyrometallurgical, hydrometallurgical and solar-driven recycling of $LiCoO_2$.

Parameters	Pyrometallurgy	Hydrometallurgy	**Solar-driven recycling (this work)**
Temperature	800-1700 °C	60-90 °C	**80 °C**
Heating source	Fossil fuel	Electricity	**Solar energy**
Chemicals	\	Conc. H_2SO_4/HCl Conc. H_2O_2	**Diluted acetic acid** **1-Octanol**
CO_2 emission (for 5 kg $LiCoO_2$)	24-27 kg	2.3-3.5 kg	**Near-zero**
Waste generation	Flue gas (NO_x, SO_x)	Acidic wastewater	**Acidic wastewater**
Hazards	Harmful gas emission	Strong acid corrosion	\

To illustrate the environmental benefits of solar-driven recycling processes, a quantitative comparison was performed with traditional approaches. A treatment amount of 5 kg $LiCoO_2$ was chosen for comparison, representing the current monthly processing capacity of the solar-driven system described in the manuscript. Typically, pyrometallurgy mainly relies on coal combustion to maintain high temperatures exceeding 1000 °C, which results in a substantial carbon footprint of approximately 24-27 kg of CO_2 for recycling 5 kg of $LiCoO_2$, as estimated from the coal demand for high-temperature operation using the GREET model (https://greet.anl.gov/). While hydrometallurgy operates at lower temperatures (60-90 °C), it necessitates the use of concentrated strong acids (e.g. H_2SO_4, HCl) and commercial H_2O_2 stock, with the electricity required for reactor heating estimated at 6-9 kWh (*Nat. Sustain.*, **2019**, *2*, 148-156). Based on the U.S. Energy Information Administration (0.388 kg of CO_2 emissions per kWh), this equates to a carbon emission of 2.3-3.5 kg (https://www.eia.gov/tools/faqs/faq.php?id=74&t=11). In contrast, our strategy utilizes solar energy to

simultaneously drive reducing agent generation and system heating, resulting in near-zero carbon emission. To facilitate a more direct comparison of these methodologies, we have summarized the key metrics in Supplementary Table 1. This comparison highlights the significant environmental benefits of our proposed solar-driven strategy.

Supplementary Note: Technoeconomic Analysis

To evaluate the economic feasibility of our solar-driven recycling process of LIB cathode materials, a technoeconomic analysis was conducted based on the proposed panel reactor (Supplementary Fig. 22) and data collected from the 30-day outdoor trial experiments. The analysis focuses on determining the levelized cost of the product (LCP) and the end-of-life net present value (NPV). The proposed panel reactor features an irradiation area of 1 m^2 and a solution volume of 0.2 m^3, with equal volumes of organic and aqueous phases. It is assumed to have a minimum operational lifetime of 10 years.

Monthly revenue

Taking real-world weather conditions in account, the average monthly effective irradiation period is assumed to be 15 days.

Based on the solution volume (200 L) of the proposed model reactor, the amount of recycled $LiCoO_2$ per month is estimated to be 5 kg. Assuming a 90% conversion efficiency, the monthly yield of $CoC_2O_4 \cdot 2H_2O$ is 8.4 kg, and the monthly yield of Li_2CO_3 is 1.7 kg.

Correspondingly, monthly revenue = 8.4 kg × 110 \$/kg + 1.7 kg × 118 \$/kg = 1124.6 \$/month.

Current market prices of $CoC_2O_4 \cdot 2H_2O$ and Li_2CO_3 are obtained from the websites: https://www.asianmetal.com/Cobalt-Oxalate-Price-Index/, https://www.metal.com/Lithium/201102250059.

Monthly cost

A comprehensive cost analysis of our solar-driven closed-loop recycling system was performed through detailed accounting of each processing step.

1. Battery acquisition and pretreatment

Based on recent literature, processing 5 kg of $LiCoO_2$ necessitates 15 kg of spent batteries (*Nat. Sustain.* **2023**, 6, 797-805). The current market price for spent $LiCoO_2$ batteries is reported at 5.6 \$/kg (*Nat.*

Chem. Eng. **2025**, 2, 142-151).

The monthly battery acquisition cost = 15 kg × 5.6 $/kg = 84.0 $/month.

According to the EverBatt2020 database (https://www.anl.gov/amd/everbatt), the cost associated with disassembly and pretreatment of spent batteries is 2.3 $/kg. Accordingly, monthly battery pretreatment cost = 15 kg × 2.3 $/kg = 34.5 $/month.

The total cost for battery acquisition and pretreatment per month = 84.0 $/month + 34.5 $/month = 118.5 $/month

2. Metal precipitation

To ensure complete precipitation of metal ions from the monthly leachate, 7.7 kg of $H_2C_2O_4$ and 251.3 kg of Na_2CO_3 are required, in addition to standard unit operations such as stirring, heating, and filtration. The involved chemical prices are obtained from https://www.intratec.us/solutions/primary-commodity-prices/commodity/oxalic-acid-prices and https://www.alchempro.com/chemical-prices/sodium-carbonate-price-insights. Metal ion precipitation is scheduled on a 3-day cycle, allowing for the processing of 10 batches per month. The price of electricity is assumed to be 0.05 $ kWh^{-1} (*Nat. Sustain.* **2023**, *6*, 827-837; *Chem Catal.* **2022**, *2*, 1720-1733). The power ratings of the instruments required for stirring, heating, and filtration are 0.0125, 0.8, and 0.1 kW, respectively, based on values reported in recent literature (*Nat. Energy* **2023**, *8*, 1137-1144).

Cost of metal precipitation per month = Cost of chemicals ($) + cost of electricity ($) = (7.7 kg × 0. 37 $/kg + 251.3 kg × 0.12 $/kg) + (0.0125 kW × 0.5 h + 0.8 kW × 2 h + 0.1 kW × 1 h) × 10 × 0.05 $/kWh = 33.8 $

3. Solar-driven metal leaching

3.1 Capital cost

The capital cost encompasses expenditures for facilities (photoreactor, Fresnel lens, and peristaltic pumps), photocatalyst, and the organic solvent (1-octanol). The prices for all aforementioned facilities are obtained from commercial online vendors (https://www.amazon.com/ and https://b2b.baidu.com).

The calculation details are presented as follows:

(1) Facility costs

Cost of photoreactor ($) = 490 $

Cost of Fresnel lens (2 m^2) ($) = 136 $

Cost of peristaltic pumps ($) = 68 $ × 2 = 136 $

Thus, the monthly facility cost, amortized over its lifetime, is calculated as follows:

Cost of facility per month = cost of facility ($) / lifetime (month) = (490 $ + 136 $ + 136 $) / 120 month = 6.4 $/month

(2) Photocatalyst dispersion costs

The photocatalyst is dispersed in 1-octanol at a concentration of 2 g/L, consistent with our outdoor experimental parameters. For the proposed model reactor, which contains a total solution volume of 0.2 m^3 (comprising equal volumes of organic and aqueous phases), this necessitates 0.2 kg of TpTz and 100 L of 1-octanol. Specifically, the cost of the photocatalyst is determined based on the yield and the market prices of the raw materials and solvents used, including DABDT (0.11 kg, 7500 $/kg), HBTP (0.12 kg, 12200 $/kg), 4-formylphenylboronic acid (0.23 kg, 440 $/kg), K_2CO_3 (0.21 kg, 1.0 $/kg), $Pd(PPh_3)_4$ (0.06 kg, 3910 $/kg), 1,4-dioxane (1.14 kg, 1.71 $/kg) and DMF (36.38 kg, 0.41 $/kg) (https://www.chemicalbook.com). The operating power for synthesis is determined to be 0.8 kW based on reported literature (*Nat. Commun.* **2024**, *15*, 8023). The price of 1-octanol is 1.96 $/L (https://www.chemicalbook.com).

Given a presumed replacement interval for the photocatalyst dispersion after a cumulative 6-month irradiation duration, its monthly cost can be determined as follows:

Cost of photocatalyst dispersion per month ($) = cost of photocatalyst ($) + cost of 1-octanol ($) / lifetime (month) = (cost of chemicals ($) + cost of electricity ($)) + cost of 1-octanol ($) / lifetime (month) = (0.11 kg × 7500 $/kg + 0.12 kg × 12200 $/kg + 0.23 kg × 440 $/kg + 0.21 kg ×1 $/kg + 0.06 kg × 3910 $/kg + 1.14 kg × 1.71 $/kg + 36.38 kg × 0.41 $/kg + 0.8 kW × 96 h × 0.05 $/kWh) + (100

L × 1.96 $/L) / 6 month = (2645.7 $ + 196 $) / 6 month = 473.6 $/month

3.2 Operational cost

Aqueous phase

In an envisioned continuous flow system, the aqueous phase, consisting of water and acetic acid, will necessitate replenishment twice daily. This frequent replenishment is crucial for maintaining a consistently low Co^{2+} concentration, which is vital to prevent H_2O_2 decomposition as demonstrated in our manuscript. This operational requirement translates to a daily consumption of 200 L of 0.6 M acetic acid solution. Considering the price of acetic acid (0.36 $/L) and water (0.00056 $/L) (https://www.echemi.com/productsInformation/temppid160628000977-acetic-acid.html, https://www.h2o-china.com/price/index), the monthly cost of aqueous phase is estimated as follows:

Monthly cost of aqueous phase ($) = cost of water ($) + cost of acetic acid ($) = 15 days × 193.4 L × 0.00056 $/L + 15 days × 6.6 L × 0.36 $/L = 37.2 $/month

The monthly cost of the solar-driven leaching system ($) = 6.4 $/month + 473.6 $/month + 37.2 $/month = 517.2 $/month

On the basis of above calculation, the overall monthly cost for the entire recycling processes (LCP) = cost of battery acquisition and pretreatment ($/month) + cost of metal precipitation ($/month) + cost of solar-driven metal leaching ($/month) = 118.5 $/month + 33.8 $/month + 517.2 $/month = 669.5 $/month

The profit per month = revenue per month ($/month) – LCP per month ($/month) = 1124.6 $/month – 669.5 $/month = 455.1 $/month

NPV analysis

Based on the calculated LCP and revenue above, the NPV can be presented as follows (where *t* represents the operational time in months):

NPV ($) = revenue over *t* months ($) – cost over *t* months ($)

= revenue over *t* months ($) – (cost of battery acquisition and pretreatment over *t* months ($) + cost of metal precipitation over *t* months ($) + solar-driven metal leaching over *t* months ($))

= revenue over *t* months ($) – (cost of battery acquisition and pretreatment over *t* months ($) + cost of metal precipitation over *t* months ($) + cost of facilities ($) + cost of photocatalyst dispersion over *t* months ($) + cost of aqueous phase over *t* months ($))

= 1124.6 $/month × *t* month – (118.5 $ × *t* month + 33.8 $ × *t* month + 490 $ + 136 $ + 136 $ + 473.6 $ × *t* month + 37.2 $/month × *t* month)

= 461.5 $ × *t* month – 762 $